

Claremont Colleges

Scholarship @ Claremont

Scripps Senior Theses

Scripps Student Scholarship

2022

Using powder diffraction to give insight into structures of Ir₂(diisocyanomethane)₄X₂ [dimen] (X = Cl; PF₆; BPh₄)

Mairead Brownell

Follow this and additional works at: https://scholarship.claremont.edu/scripps_theses

 Part of the [Atomic, Molecular and Optical Physics Commons](#), [Inorganic Chemistry Commons](#), [Materials Chemistry Commons](#), and the [Physical Chemistry Commons](#)

Recommended Citation

Brownell, Mairead, "Using powder diffraction to give insight into structures of Ir₂(diisocyanomethane)₄X₂ [dimen] (X = Cl; PF₆; BPh₄)" (2022). *Scripps Senior Theses*. 1827. https://scholarship.claremont.edu/scripps_theses/1827

This Open Access Senior Thesis is brought to you for free and open access by the Scripps Student Scholarship at Scholarship @ Claremont. It has been accepted for inclusion in Scripps Senior Theses by an authorized administrator of Scholarship @ Claremont. For more information, please contact scholarship@cuc.claremont.edu.

Using powder diffraction to give insight into structures of $\text{Ir}_2(\text{diisocyanomethane})_4\text{X}_2$ [dimen]

(X = Cl; PF_6 ; BPh_4)

A Thesis Presented

by

Mairead Redmond Brownell

To the Keck Science Department

of

Claremont McKenna, Scripps, and Pitzer Colleges

In Partial Fulfillment of

The Degree of Bachelor of Arts

Senior Thesis in Chemistry

April 25, 2022

Acknowledgements

I would first like to thank my primary advisor, Natalia Powers-Riggs, for always being there for me and for challenging me to be a better chemist. Natalia, I can't thank you enough for taking me under your wing in the last year and being so supportive in every step of the research, experimentation, and writing of my thesis. I will never forget riding bikes around APS at midnight and looking at all the cool research that was being conducted. You have been such an inspiration to me as both a chemist and a person, and I will be forever grateful to have you as a mentor.

I would also like to thank my first reader, Nancy Williams, and my second reader and academic advisor, Beth Caulkins. Nancy, thank you so much for all your guidance throughout my thesis. Thank you also for helping me grow into a better scientific writer and challenging me to see the bigger picture of my thesis project. Beth, thank you, not only for reassuring me throughout my thesis, but for reassuring me through my entire time at Scripps. You were my first chemistry professor in college and always made me feel so welcome when I felt out of place in a new state. Since then, I have learned so much from you about chemistry but also about being a compassionate leader and mentor.

I also have to thank all of the professors who have fostered my growth as a chemist and student during my time in college. Dr. Otte, Professor Purvis-Roberts, Professor Vaughn, Professor Black, Professor Berkolds, Professor Kamm, thank you for pushing me to be a better student, learner, and leader.

I want to thank the U.S. Department of Energy, SLAC National Laboratory, Argonne National Laboratory and everyone I worked with over the summer for providing me with the best research experience I could have hoped for. I especially want to thank Dr. Amy Cordones-Hahn and Dr. Kelly Gaffney for welcoming me into the lab, Dr. Olaf Borkiewicz for being so helpful

while we were at APS, and all of the post-docs who gave me invaluable advice regarding graduate school and research.

Finally, I have to thank my friends and family for always believing in me and encouraging me throughout my education. Nana and Granda, thank you for being there for me all last summer while I was working at SLAC. Aidan and Ruari, thank you for being the best brothers I could ever ask for. Dad, thank you for supporting me in all my endeavors. Mom, thank you for challenging me to be the person and the student I am today. Thank you for everything and I love you so much.

Table of Contents

Acknowledgements.....	2
Abstract.....	6
Introduction.....	7
Electronics and Structure.....	7
I. Hydrogen as a source of fuel.....	7
II. Transition metal complexes as photocatalysts.....	8
III. d ⁸ -dimers and metal-metal transitions.....	9
IV. Promises and limitations of Ir ₂ (dimen) ₄ ²⁺	11
i. Structure and geometry of Ir ₂ (dimen) ₄ ²⁺	11
ii. Metal-metal transitions in Ir ₂ (dimen) ₄ ²⁺	13
iii. Temperature dependence of Ir ₂ (dimen) ₄ ²⁺	13
X-Ray Diffraction.....	14
V. X-ray scattering.....	14
VI. Young's double slit experiment.....	14
VII. Bragg's Law.....	17
VIII. Unit Cells.....	20
IX. Synchrotrons.....	23
Methods.....	25
I. General considerations.....	25
II. Synthesis of Ir ₂ (dimen) ₄ ²⁺	25
i. [Ir ₂ (dimen) ₄][Cl] ₂	25
ii. [Ir ₂ (dimen) ₄][PF ₆] ₂	25

iii. $[\text{Ir}_2(\text{dimen})_4][[\text{BPh}_4]_2]$	26
III. Loading samples and collecting diffraction patterns.....	27
IV. Analysis of observed diffraction patterns in solid samples.....	27
i. Plotting scattering curves.....	27
ii. Analyzing scattering curves.....	27
Results and Discussion.....	28
I. Experimental Scattering of $[\text{Ir}_2(\text{dimen})_4][\text{X}]_2$ at Beamline 11-ID-B.....	28
II. $[\text{Ir}_2(\text{dimen})_4][\text{PF}_6]_2$	28
III. $[\text{Ir}_2(\text{dimen})_4][\text{BPh}_4]_2$	31
Conclusion.....	35
References.....	37

Abstract

$\text{Ir}_2(\text{dimen})_4^{2+}$ (dimen = 1,8-diisocyanomenthane) has been studied extensively as model compound to better understand catalysis of photochemical reactions. Although $\text{Ir}_2(\text{dimen})_4^{2+}$ has been used primarily to observe the photophysical changes of metal-metal transitions, it gives great insight into the transitions that allow other d^8 - d^8 metal complexes to undergo photochemical processes and generate hydrogen gas. The large visible range by which $\text{Ir}_2(\text{dimen})_4^{2+}$ (**1**) can be electronically excited in solution is indicative of its two solution phase ground states, which interestingly have been hypothesized to resemble two unique packing structures observed in the powder state. In this study, the powder diffraction patterns of $[\text{Ir}_2(\text{dimen})_4][\text{Cl}]_2$ (**1-Cl**), $[\text{Ir}_2(\text{dimen})_4][\text{PF}_6]_2$ (**1-PF₆**), and $[\text{Ir}_2(\text{dimen})_4][\text{BPh}_4]_2$ (**1-BPh₄**) powders were investigated via X-ray diffraction. The resulting curves were compared to published data and other potential unit cells were generated for the crystalline powder samples. **1-PF₆** and **1-BPh₄** were determined to have quite different packing structures and symmetries, and while the scattering curve of **1-PF₆** matched the previous literature spectrum well, the scattering curve of **1-BPh₄** differed quite drastically from the previous literature spectrum. A unit cell could not be determined for any of the species, but a couple of new cells are proposed.

Introduction

Electronics and Structure

I. Hydrogen gas as a source of fuel

Discovering new, greener methods of generating and storing useful energy is crucial in a time where emissions have increased, and continue to increase, global climate change at a rate unseen in Earth's history. Fossil fuels, which comprise the majority of the fuel used worldwide, significantly contribute to Earth's climate and global warming. Fossil fuels contribute to global warming because they form carbon dioxide and water when combusted. Because of this, scientists have invested significant energy and resources in determining new, greener sources of fuel. One source of fuel that has shown promise is hydrogen gas.¹ Unlike fossil fuels, hydrogen gas combusts to form water, thus making it a greener alternative to fossil fuels.¹

While hydrogen gas shows promise as a fuel, the synthesis of hydrogen gas is currently carried out almost exclusively with the use of fossil fuels, defeating its utility as an *alternative* to fossil fuels.² The most promising mechanism to generate hydrogen gas without the use of fossil fuels is by using solar energy to split water or synthesizing hydrogen gas through other hydrogen-evolving mechanisms.^{1,3} Unfortunately, the kinetic barriers to this reaction are such that a catalyst is necessary to effect it.¹ Transition metal complexes have shown great promise as hydrogen-evolving catalysts.⁴ However, transition metal complexes must possess a variety of specific qualities in order to provide the necessary conditions for catalyzing water into hydrogen gas.¹

II. Transition metal complexes as photo-catalysts

Metal complexes have displayed promising characteristics that may allow for the efficient photocatalysis of hydrogen-evolving reactions. All compounds possess the ability to be electronically excited by some wavelength of light.⁵ These transitions can occur at a variety of wavelengths, including those that occur in the visible region, which compose about 40% of solar waves that permeate the Earth's atmosphere.⁶ Many transition metals are capable of photoexcitation in this critical region, in strong contrast to the large majority of more traditional organic frameworks.⁷⁻⁹ Excitation of these metal complexes can also allow for a variety of other photophysical processes, such as isomerization, to take place, potentially improving catalysis.

When excited by visible light, compounds undergo an electronic transition that causes one electron to be excited into a new orbital.^{3,9,10} In most cases, the electron excited into the new orbital originates from an orbital containing two electrons with opposite spin.³ The electron is thereby excited into a singlet excited state, which means it retains its spin when excited.^{3,7} The singlet excited state is generally extremely short-lived, thus giving the metal complex very little time to catalyze reactions.^{3,7,11} However, electrons in the excited singlet state have the ability to undergo intersystem crossing, which causes the spin of the electron in the excited state to change its spin to align with that of the electron from the highest occupied molecular orbital, forming a triplet state.^{3,7,12} The triplet state exists at a lower energy than the singlet state, but has a longer lifetime; since excited states are often catalytically active, excitation followed by intersystem crossing is a potentially useful strategy for enhancing catalysis.^{2,3,8}

There are many proposed mechanisms for metal-catalyzed hydrogen evolution. A number of these methods involve a pathway in which the metal complex is excited by visible light and then reduces protons to molecular hydrogen.¹ The oxidized metal complex can then be reduced by

a number of pathways to complete the catalytic cycle.¹ One class of complexes that have been investigated in the context of this type of mechanism are binuclear d^8 square planar complexes. These complexes have a number of specifications. First, the metal complex must be binuclear and the ligands must act as bridges between the two metal nuclei.^{3,10} Second, they must possess square planar geometry, thus causing the d -orbitals in the z -plane to lower in energy.^{3,10,13,14} Finally, the metal must be a d^8 complex.³ This means that there are eight electrons in the non-bonding d -orbitals.^{13,14} These characteristics consequently cause the highest energy electrons to fall into the d_{z^2} orbital. Then, when you consider the two metal atoms in the complex simultaneously, the molecular orbital diagram displays the HOMO in the $d\sigma^*$ -antibonding orbital, thus making the LUMO the $p\sigma$ -bonding orbital.³

III. d^8 -dimers and metal-metal transitions

d^8 transition metal complexes of the second and third row containing metals like platinum(II), gold(III), iridium(I), palladium(II), and rhodium(I) generally exhibit square planar geometry.^{13,14} This means that each ligand is bonded to the metal atom such that each cis ligand-metal-ligand bond angle is about 90° , thus making the geometry surrounding the metal atom planar. Metal complexes with this geometry exhibit unique electronic structures where the d -orbitals in the z -plane drop in energy while d -orbitals in the xy -plane increase in energy, thus causing the d -orbitals to exhibit four distinct energies and only two degenerate orbitals.^{3,13} In d^8 dimers, the eight non-bonding electrons fill the d_{xy} , d_{yz} , d_{xz} , and d_{z^2} leaving $d_{x^2-y^2}$ vacant.

When two such complexes are brought together, the resultant MO diagram is shown in Figure 1.

In this molecular orbital diagram, the d_{z^2} orbitals form a bonding and antibonding pair of orbitals and the four electrons are filled such that the HOMO becomes the $d\sigma^*$ -antibonding orbital (Figures 1-2).^{3,7} Similarly, the p_z orbitals also form a bonding and antibonding pair of orbitals.^{3,8} The $p\sigma$ bonding orbital thus becomes

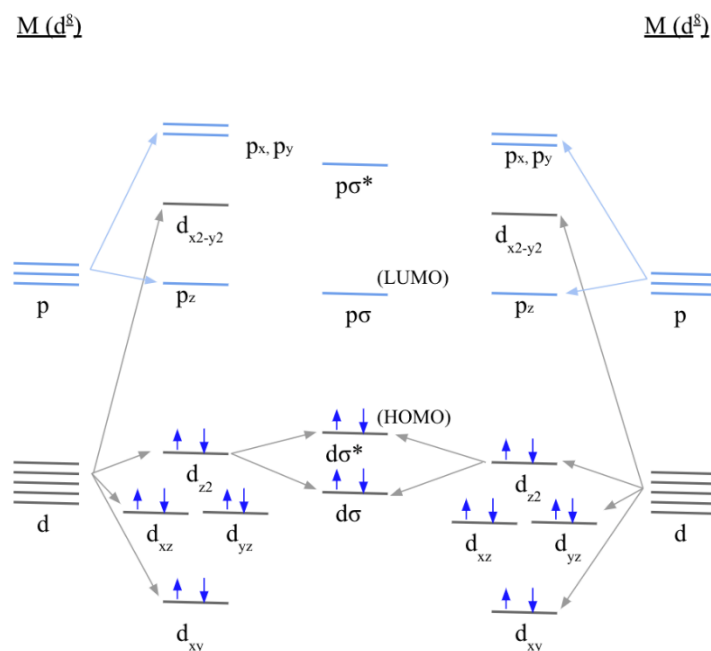


Figure 1. The molecular orbital diagram showing the HOMO and LUMO of the metal-metal interaction in d^8 - d^8 square planar dimers.²

the LUMO and the HOMO-LUMO gap lies at an energy level such that it can be accessed by visible light (Figures 1-2).^{3,8}

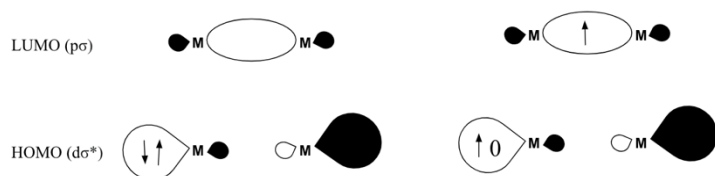


Figure 2. A figure showing the general shape of the highest occupied molecular orbital (HOMO) and the lowest unoccupied molecular orbital (LUMO) of the metal-metal transition that occurs in d^8 binuclear complexes.

Given this electronic structure, in the ground state the metal-metal bond interaction has a bond order of 0 (Figure 2).^{3,8,13} However, when an electron from the $d\sigma^*$ -antibonding HOMO is excited

into the $p(\sigma)$ LUMO, causing the M-M bond order to increase to 1 (Figure 2).

This electronic transition has been shown to catalyze reactions to generate hydrogen gas in examples such as the platinum catalyst, Pt(pop), which has been shown to reduce to a d^7-d^7 metal catalyst when catalyzing hydrogen-evolving reactions.^{15,16}

IV. Promises and limitations of $\text{Ir}_2(\text{dimen})_4^{2+}$

Structure and geometry of $\text{Ir}_2(\text{dimen})_4^{2+}$ in the ground and excited states

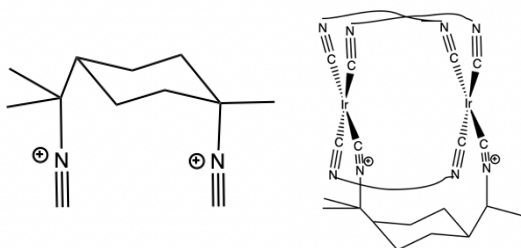


Figure 3. Structure of a) diisocyanomethane (dimen) and b) $\text{Ir}_2(\text{dimen})_4^{2+}$. There are four dimen ligands bonded to the iridium atoms, but for the sake of simplicity, only one is shown here.

One d^8 -square planar dimer complex, $\text{Ir}_2(\text{dimen})_4^{2+}$ (**1**), consists of two iridium atoms, each bonded to the terminal carbon atoms of four 1,8-diisocyanomethane (dimen) molecules (Figure 3).¹⁰ As a d^8 square planar dimer, **1** undergoes a $d\sigma^*-p\sigma$ transition when excited by visible light.^{3,7} While the photochemical capabilities of **1** to catalyze

hydrogen-evolving reactions have not yet been investigated, the photophysical properties of these complexes are particularly interesting and give important insight into the nature of the metal-metal transitions and intersystem crossing that can enhance photochemical catalysis.

$\text{Ir}_2(\text{dimen})_4^{2+}$ (**1**) exhibits two conformers in the ground state, one with a short, twisted shape and the other with a long, eclipsed shape (Figure 4).^{7,8,10} This was reported by Gray, *et al.*, who used X-ray diffraction to determine that **1** packs in a short and twisted conformer when precipitated with a tetraphenyl borate counterion and a long, eclipsed conformer when precipitated with hexafluorophosphate.⁷ The short, twisted conformer has a metal-metal distance of 3.60 Å while the long, eclipsed conformer has metal-metal distance of 4.41 Å.^{7,10} When the UV-visible spectrum of the crystal structures were obtained, the long, eclipsed conformer was determined to absorb visible light primarily at 585 nm while the short and twisted conformer was determined to absorb at 480 nm.^{8,10}

Interestingly, the UV-visible absorption spectrum of **1** in solution exhibits two peaks at 585

nm and 480 nm, thus suggesting that both conformers exist in equilibrium in solution.⁹ These two ground states are of particular interest in understanding the photophysical characteristics of **1** and why it exhibits both ground states in solution. It also means that **1** absorbs at wavelengths that span the visible spectrum from 480 nm to 585 nm. Because photoelectronic excitations span the majority of visible spectrum, this finding is of particular interest to better understanding the photophysical properties of **1** and other d^8 square planar transition metal dimers, thus allowing for increased understanding of the catalytic system as a whole.

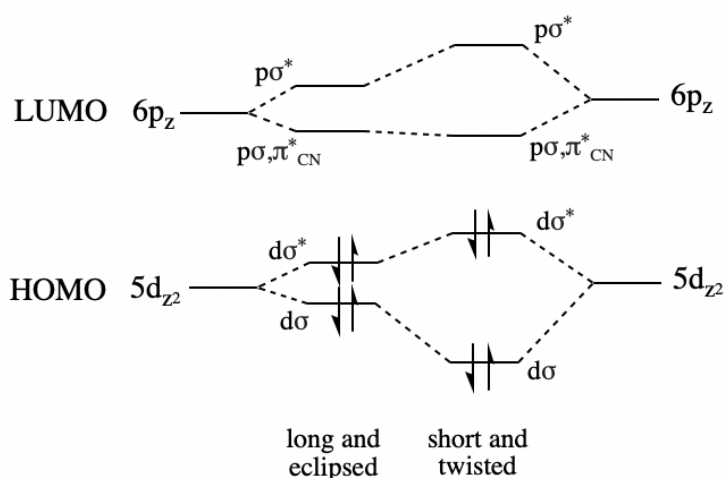


Figure 4. Energy diagram showing the HOMO and LUMO of $\text{Ir}_2(\text{dimen})_4^{2+}$ in the two observed ground states.

Metal-metal transitions in $\text{Ir}_2(\text{dimen})_4^{2+}$

Ir (I) is a d^8 metal center, so the d -orbitals are all filled save the 5 $d_{x^2-y^2}$, and both the 5 d_{z^2} and 6 p_z are formally non-bonding.^{3,8} When two such centers are brought together, each of these pairs of orbitals form a bonding-antibonding pair, with $5d_z\sigma$ and $5d_z\sigma^*$ both filled (the latter forming either the HOMO or a frontier orbital close in energy to the HOMO) and the $6p_z\sigma$ and $6p_z\sigma^*$ being empty (the former either being the LUMO or a frontier orbital close in energy to the LUMO) (Figure 4).⁸ Thus, one possible excitation is the $5d_z\sigma^* \rightarrow 6p_z\sigma$ transition. This results in a weak metal-metal bond and causes the metal-metal distance to shorten. Interestingly, this excited state is observed when both the short, twisted conformer and the long, eclipsed conformer are excited, despite the fact that they have different ground state energies (Figure 4).⁸

Temperature dependence of $\text{Ir}_2(\text{dimen})_4^{2+}$

In solution, $\text{Ir}_2(\text{dimen})_4^{2+}$ (**1**) in solution exhibits two peaks at 480 nm and 585 nm, corresponding to the short, twisted and long, eclipsed isomers, respectively.⁹ Interestingly, Hunter *et al.* showed that the absorbance at 585 nm decreases while the absorbance at 480 nm increases as temperature increases from 150 K to 296.8 K.⁹

Because of these intriguing results, we endeavored to obtain high-quality solid-state information about the structure of the isomers via X-ray diffraction.

X-Ray Diffraction

V. X-Ray Scattering

Unlike lower-energy photons, high-energy X-rays cannot be absorbed by most compounds. Instead, when X-rays interact with electrons, they typically cause scattering.^{17,18} In X-ray scattering, X-ray waves of a specific frequency are incident on a sample at some angle. The waves are then refracted off the sample. After light is scattered, these waves interact either constructively or destructively with one another, much like photon behavior in Young's double-slit experiment.^{19,20} When a sample is crystalline, the scattered waves result in a pattern that can be used to determine structural characteristics of the compound being tested (Figure 5).^{17,18}

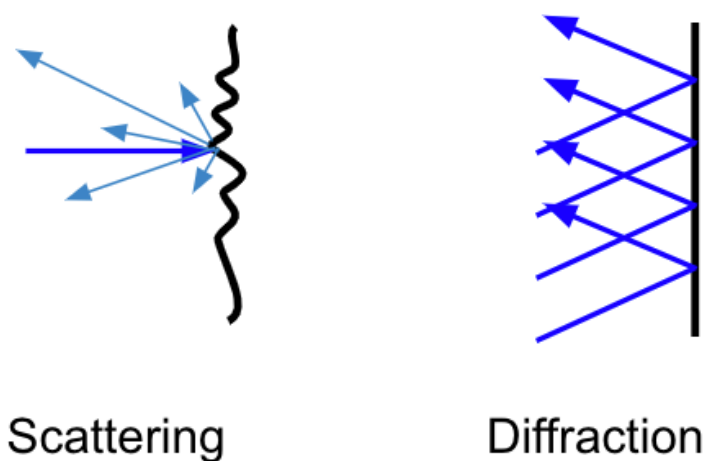


Figure 5. A schematic showing generalized wave propagation patterns in scattering and diffraction.

VI. The Double-Slit Experiment

In the double-slit experiment, a light source and a detector are separated by a filter with two small slits, with a width approximately equal to the wavelength of light. Young hypothesized that, when the light source was allowed to run for some time, he would observe two lines of equal

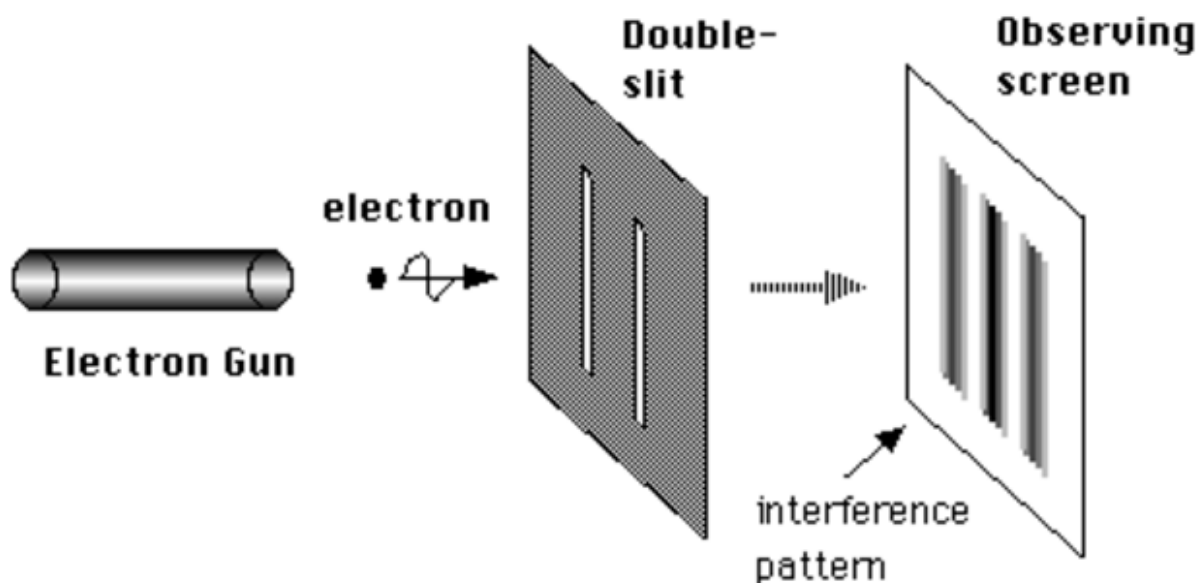
intensity on the detector directly opposite of the locations of the slits.^{19,20} Surprisingly, Young observed several bands on the detector with varying intensities, indicating an interference pattern (Figure 6).^{19,20} These results prompted Young and other physicists to hypothesize that, rather than electrons behaving simply as particles, they also behave as waves that interact constructively and destructively to give the unexpected experimentally determined pattern that Young observed.^{19,20} These results were thus used to develop the wave-particle duality theory of light particles that exists today.

The double-slit experiment has been altered and reproduced since the development of the wave-particle duality theory. One interesting and applicable extension of the initial double slit experiment was later conducted by Young and is still used to structurally characterize substances with X-rays. In this experiment, Young used the same setup as in his original double-slit experiment. However, instead of keeping the distance between the slits constant, he altered the distance between slits and observed how changing the distance between slits impacted the detected interference pattern.²⁰ Young determined that, as slit distance decreased, the distance between constructive interference patterns increased. This relationship is expressed through the equation,

$$d = \frac{\lambda r}{s} \quad (1)$$

where d is the distance between the slits, λ is the wavelength of incident light, r is the distance from the slits to the detector, and s is the distance between slits.²⁰ If we think about this in the context of atoms, when two atoms with equal electron density are close together and are exposed

to a high energy light source, they exhibit constructive interference whose spacing is greater than that of atoms who have more space between each other.



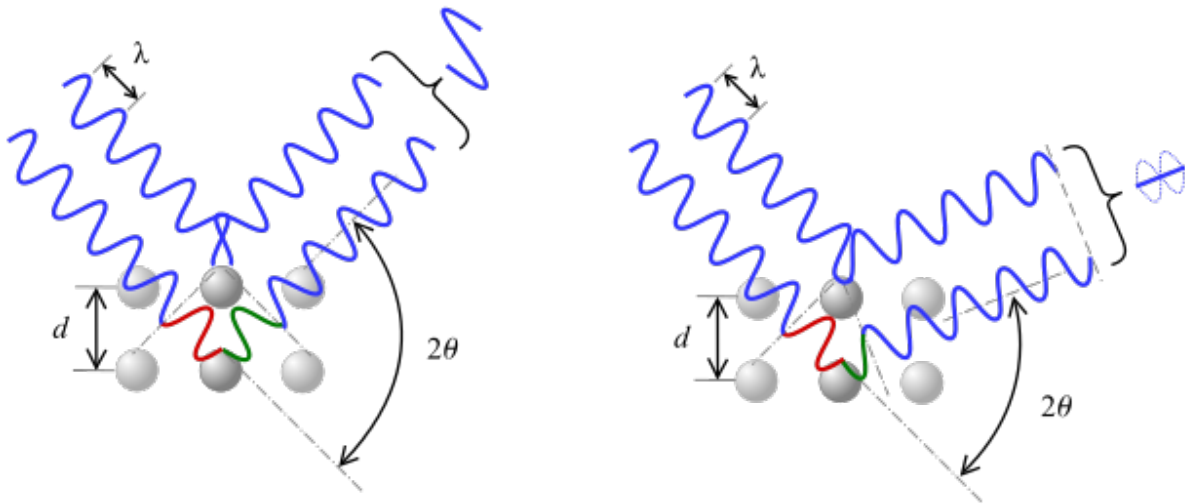
Taken from NekoJaNekoJa-commonswiki via <http://commons.wikimedia.org/w/index.php?search=double+slit+experiment&title=Special:MediaSearch&go=Go&type=image>

Figure 6. Schematic showing the set up and results of the double slit experiment.²¹

Young's experiments have been adapted and modernized through time to produce the modern role of light scattering in determining the structure of compounds. Similar to the double slit experiment, X-ray diffraction depends on the interference of light waves after diffraction off of a surface. However, unlike Young's experiment where much lower energy light waves were allowed to interact with much larger slits, patterns resulting from X-ray diffraction are the result of diffraction off of a crystalline, layered substance with spaces corresponding to inter-atomic distances. Deflection of light off of atoms in a regularly repeating structure can lead to constructive or destructive interference, a phenomenon described by Bragg's Law.^{17,18}

VII. Bragg's Law

Bragg's Law provides us with a way to translate scattering intensities and phase changes to interatomic distances based off assumptions made about packing within a sample. In order to do this, a sample is first exposed to an X-ray beam with a defined wavelength. After being diffracted off a 3-dimensional sample, the waves interact either constructively or destructively to create a pattern on a detector that can be analyzed to determine structural features of the crystalline samples (Figure 7).^{17,18,22,23} Similar to the orientation of waves when they passed through the slits in Young's double slit experiment, the waves that are diffracted off of various atoms at differing angles and phases, consequently making a pattern based off the orientation of the waves when they interact with a detector. However, unlike Young's experiment where waves were allowed to interact soon after being emitted from the light source, X-ray diffraction is detected after the waves are allowed to diffract off of electron density in the sample, thus making the scattering pattern unique to each sample and dependent on the sample's structure (Figure 7).^{17,23}



Taken from Cdang via <https://commons.wikimedia.org/w/index.php?search=bragg%27s+law&title=Special:MediaSearch&go=Go&type=image>

Figure 7. A diagram showing the function of Bragg's Law in a two-dimensional sample where two waves are diffracting off of two different planes and thus interacting with different phases upon diffraction.²⁴

In 3-dimensional compounds, diffraction can occur at any location in the complex, not merely at the very surface. Because of this, a more complex theory of wave interaction must be introduced. Therefore, in complex, 3-D systems, Bragg's Law is used to best describe wave interactions after diffracting off a surface. Bragg's Law is written as,

$$n\lambda = 2d \sin\theta \quad (2)$$

where λ is the incident wavelength, θ is the angle at which light hits the sample, and d , similar to equation (1), is the distance between planes or, more simply, atoms.¹⁷ Additionally, n is an integer called the diffraction mode, which is indicative of the difference in phase between wavelengths interacting following diffraction. After X-ray waves are incident on a sample, they are diffracted off electrons and interfere. As in equation (1), the distance between planes, or, more effectively, atoms, dictates the ways in which the X-rays interact following diffraction. Because of this, all structures which have unique distances between atoms cause X-rays to interact uniquely after being diffracted off of them.

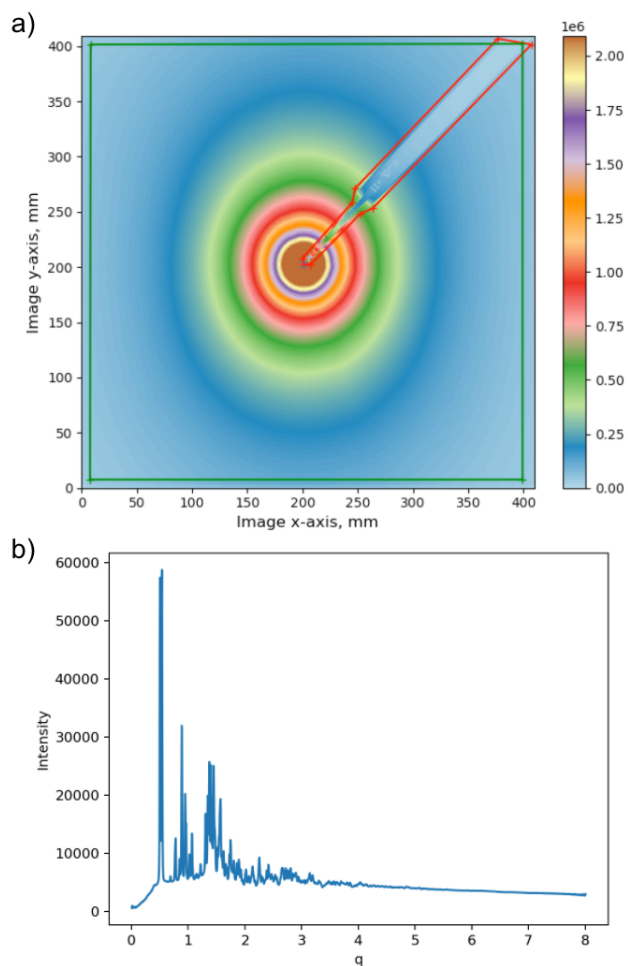


Figure 8. Figures showing a) the scattering pattern of $\text{Ir}_2(\text{dimen})_4^{2+}$ and the b) resulting scattering curve collected at beamline 11-ID-B at APS.

After the scattering pattern is collected, the intensities surrounding the detector are integrated from 0 to 2π (Figure 8).²⁵ The result is a one-dimensional scattering curve (Figure 8b). Scattering curves are displayed as plots of intensity vs 2θ , where 2θ can be interpreted as the difference between the location of the detected wave and the incident wave expressed in degrees or radians.²⁵ This 2θ value is dependent on the wavelength of the X-ray source. In order to make the curve wavelength independent, the x-axis can be converted to q-space, a non-existent space that is inversely proportional to real space (Figure 8b). This is important because, when

analyzing scattering curves extracted from beamlines with differing incident frequencies, wavelength-independent units allow us to more easily compare the observed scattering curves. Thus, the lower the value of q, the greater the intermolecular distance.²⁶ In order to convert between 2θ to q-space, the following conversion can be used:

$$|q| = \frac{4\pi}{\lambda} \cdot \sin \frac{2\theta}{2} \quad (3)$$

Lambda, λ , is equal to the wavelength of the incident X-ray beam and 2θ is equal to the two times the difference in angle between the incident X-ray beam and diffracted X-ray beam.²⁶

Because a scattering curve is dependent on waves interacting in an ordered manner, clear results from X-ray diffraction experiments require that a sample be ordered, or crystalline.^{17,18} This allows the compound to be classified using molecular symmetry, and thus such compounds must contain a unit cell (see below).

VIII. Unit Cells

When a compound is crystalline, it has a repeated orientation and packing of its atoms.^{17,18,22,27} Because of this, it can be defined using a unit cell, an abstract, 3-dimensional unit whose structure is identical to that of its neighbors. In other words, the unit cell can be translated infinitely in the x-, y-, and z-directions to obtain a structure identical to the original structure. The unit cell is the smallest portion of a structure that is translationally replicable across a crystalline sample.^{17,18,22,27} A unit cell's classification is dependent on the symmetry of that structure. Unit cells are classified by both the symmetry of the compound within the cell and the shape of the cell itself. Two unit cell classes that are of particular interest in our studies of $\text{Ir}_2(\text{dimen})_4^{2+}$ (**1**) are orthorhombic and triclinic.^{17,18} An orthorhombic unit cell has corners whose angles are all 90° and side lengths that are all different, whereas triclinic unit cells have differing side lengths and angles who are *not* equal to 90° .^{17,18,23}

Miller Planes

In a crystalline powder sample, the compound packs such that the unit cell is repeated translationally in the x-, y-, and z-directions. However, for the sake of simplicity, we will discuss the unit cell in 2-dimensions. A unit cell can further be described by lattice points as seen in Figure 9.²⁸ Similar to an xy-coordinate plane, the unit cell can be placed within lattice points such that one side is defined by x while the other is defined by y. Then, every point within the cell is some

combination of x and y that can be defined using fractions of x and y.^{17,27} The lattice points used to describe the compound and unit cell primarily aid in providing structural and atomic spacing information of the compound through the application of Bragg's

Law. To do this, lines, or one-dimensional planes, can be used to describe cross sections of the unit cell. For example, $(1x, \infty y)$ refers to

the one-dimensional plane that runs along side x while $(\infty x, 1y)$ refers to the plane in the cell that runs along side y.^{17,27,28} Inside the unit cell, planes whose dimensions are $(1/2x, \infty y)$ or $(1x, 1y)$, for example, can be used to further define locations of atoms within the cell and possible angles from which X-rays may diffract.

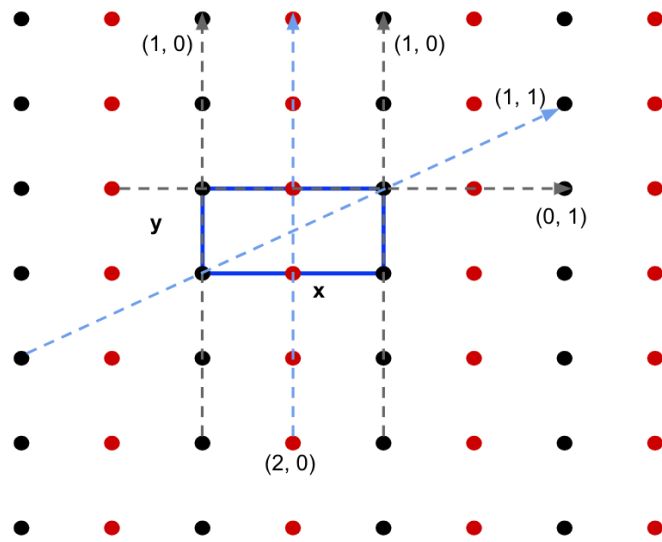


Figure 9. A figure showing lattice points and an example of a unit cell and the unit cell's $(1, 0)$, $(0, 1)$, $(2, 0)$, and $(1, 1)$ planes.²⁸ Diffraction occurs at locations of high electron density whose locations can be described using the Miller Planes like the ones sketched in this image.

In X-ray diffraction and structural determination studies, planes can be referred to simply using the fraction of the unit cell's sides rather than a function of the side itself. For example, instead of referring to a plane as the $(1/2x, \infty y)$ plane, it can simply be referred to as the $(1/2, \infty)$ plane.^{17,27} Additionally, rather than using fractions to describe the planes within the unit cell, we generally use Miller Planes.

Structural studies use Miller Planes because planes within a unit cell can exist at infinitely small fractions. To convert planes with fractions to Miller Planes, you simply take the reciprocal of the conventional plane, so the plane at $(1/2, \infty)$ then becomes $(2, 0)$, or just (20) , when using Miller planes to describe locations within the cell.^{22,27} This means that, when planes have greater x- and y-values, they are actually closer to the origin.

Remember that light is diffracted off electrons. Because planes are used to describe the location of atoms and electrons, we can say that light is diffracted off planes defined by the unit cell. When light is diffracted off planes that run through two sets of black lattice points, such as the two $(1, 0)$ planes in Figure 9, the symmetry of the unit cell causes the waves to be in phase, and thus experience constructive interference. However, when light is diffracted off a plane that runs through red lattice points and a parallel plane that runs through black lattice points, like the $(2, 0)$ plane and the $(1, 0)$ plane in Figure 9, the waves interact such that they are out of phase, thus causing destructive interference. This application of planes in unit cells is how Bragg diffraction can be applied to structural studies.

This model can be extended to 3-dimensional species, which is what we do in this project. This study aims to better understand the powder diffraction, packing, and structures of $\text{Ir}_2(\text{dimen})_4^{2+}$ (**1**) with chloride (2Cl), hexafluorophosphate (PF_6), and tetraphenylborate (BPh_4) counterions. Studying the structures of these using powder diffraction is important to further research regarding

structure analysis of **1** in solution. In order to do this, a synchrotron must be used to obtain high-energy photons and collect data.

IX. Synchrotrons

A synchrotron is a high energy X-ray source that can be used to determine a variety of electronic and structural components of compounds and macromolecules. In a synchrotron, electrons are emitted from an electron source and are then propagated circularly using an array of magnets.^{25,29} The high energy propagation of electrons around the synchrotron results in high-powered X-rays that has about 100 times more power than medical X-rays.^{25,29} Because the placement of the magnets in the synchrotron causes the electrons to propagate in a circle, altering the location of the magnets causes the X-ray beam to instead propagate tangentially away from the circular path. This occurs at every tangent around the synchrotron, and so there are several locations around each synchrotron where samples can be exposed to a beam tangential to the circularly propagated wave (Figure 10).^{25,29} In this experiment, the Advanced Photon Source at Argonne National Laboratory is used to determine the scattering curves of **1-Cl₂**, **1-PF₆**, and **1-BPh₄**.

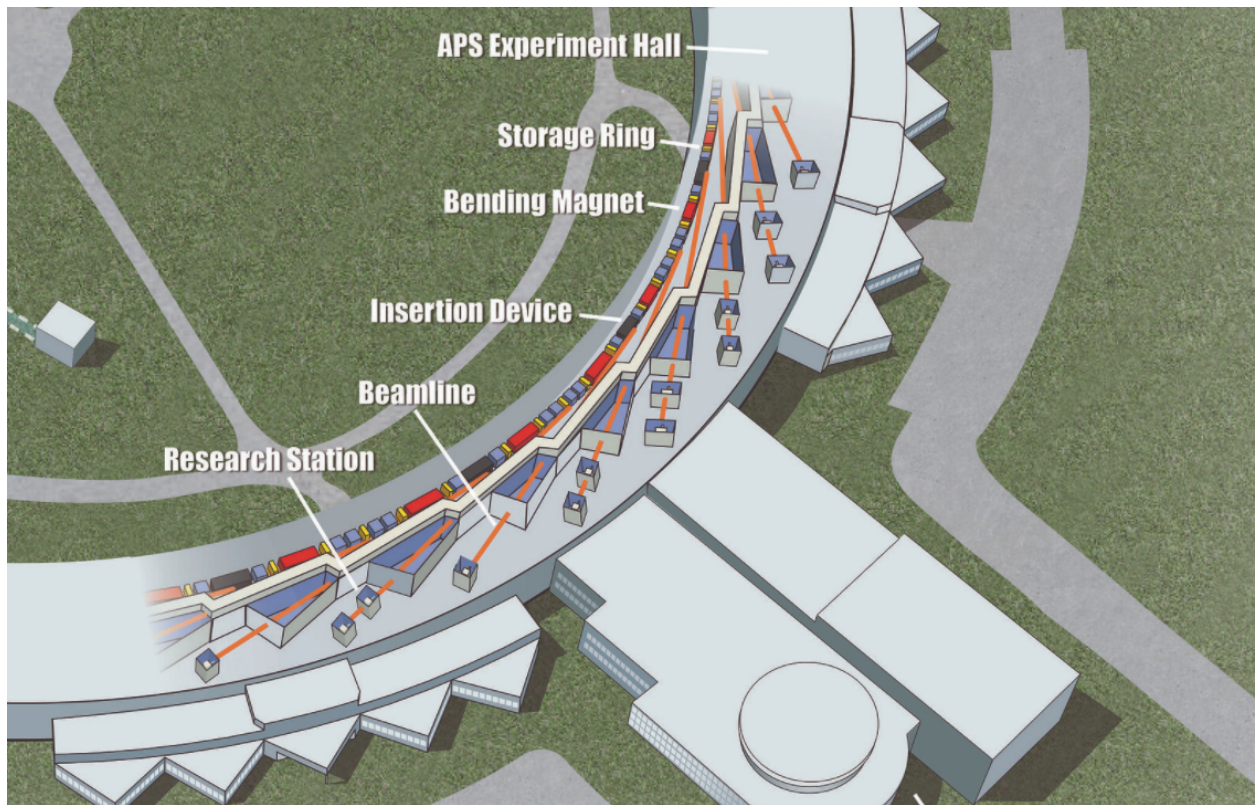


Figure 10. A cartoon showing the path of propagated waves and the beamline pathways for varying research stations.²⁹ When a beamline is in use, the X-rays are propagated tangentially from the synchrotron to the research station where the sample is exposed to the high energy beam of light.

Materials and Methods

I. General Considerations

Chemicals for this experiment were purchased from Sigma. **1-X** (**1-X** = $[\text{Ir}_2(\text{dimen})_4][\text{X}]_2$, $\text{X} = \text{Cl}$ (**1-Cl**), PF_6 (**1-PF₆**), or BPh_4 (**1-BPh₄**)) powder samples were conducted at SLAC National Laboratory under air-free conditions. They were then stored and sent to Argonne National Laboratory under air-free conditions. **1-Cl** was synthesized again at Argonne National Laboratory under ambient atmosphere. X-ray diffraction patterns were collected at sites 11-ID-B and 11-BM of Argonne National Laboratory's Advanced Photon Source (APS). Additionally, a nitrogen-filled glove box was used to store samples at APS.

II. Synthesis of 1-X for powder sample testing

Synthesis of 1-Cl

$[\text{Ir}(\text{COD})\text{Cl}]_2$ (10.1 mg, 37 μmol , COD = 1,5-cyclooctadiene) and 1,8-diisocyanomenthane (dimen, 11.5 mg, 155 μmol , 4 equiv.) were placed into two separate vials with dry, air-free dichloromethane and sparged with nitrogen for twenty minutes. The solution containing dimen was transferred to the vial containing $[\text{Ir}(\text{COD})\text{Cl}]_2$ via needle to ensure that minimal air and water entered the system. The reaction vial was swirled until it displayed a dark purple color. **1-Cl** was then precipitated by adding hexanes and allowing the blue powder to settle at the bottom of the vial. The powder was isolated using vacuum filtration and the dried powder was packaged and sent for use at APS.³⁰

Synthesis of 1-PF₆

NH_4PF_6 (30 mg, 0.21 mmol , 2 equiv.) was dissolved in 10 mL of a 1:1 water/methanol mixture. This solution was sparged with nitrogen for twenty minutes. The solution was transferred to a

nitrogen-containing vial containing **1-Cl** (18 mg, 0.015 mmol, xx equiv.). The resultant **1-PF₆** precipitate was triturated with ice water, and **1-PF₆** was isolated as a maroon solid by Büchner funnel filtration.^{30,31}

Synthesis of **1-BPh₄**

1-Cl (30 mg, 0.021 mmol) and NaBPh₄ (17 mg, 0.052 mmol, 2 equiv.) were dissolved in separate vials containing a 1:1 water/methanol mixture. This solution was degassed using a Schlenk line for 20 minutes. The solution of NaBPh₄ was transferred to a vial containing **1-Cl** via needle. The resulting **1-BPh₄** precipitate was precipitated in an ice bath, and **1-BPh₄** was isolated as a maroon solid by Büchner funnel filtration. The resulting solid samples were expunged with argon in a glove box.^{30,31}

III. Loading samples and collecting diffraction patterns

Preparing and running solid samples of **1-X**

The powder samples of **1-Cl**, **1-PF₆**, and **1-BPh₄** were placed into capillary tubes with a diameter of 1.1 mm. The samples were then inserted into the sample holder and the X-ray diffraction patterns were detected using a Perkin-Elmer flat panel detector. An incident wavelength of 58.6 keV was used at beamline 11-ID-B and 30 keV at beamline 11-BM and the sample-to-detector distance was calibrated using a CeO₂ standard.³²

IV. Analysis of observed diffraction patterns in solid samples

Plotting the scattering curves of literature crystal samples and experimental data from tested samples

The crystallographic structures of **1-PF₆** and **1-BPh₄**, published on the Cambridge Structural Database upon the publication of Gray *et al.*, were used to determine the scattering curves of the samples using a wavelength of 1.54 Å in angular space. Then, the plots were converted to reciprocal (q) space using the following equation:

$$|q| = \frac{4\pi}{\lambda} \cdot \sin \frac{2\theta}{2} \quad (3)$$

The scattering curves in both angular and reciprocal space were plotted in Jupyter Notebook.

The scattering pattern of **1-Cl**, **1-PF₆**, and **1-BPh₄** were converted to scattering curve values which were then plotted in Jupyter Notebook. The experimental scattering curves were compared to the literature scattering curves to determine whether or not the product packed with a crystal structure upon synthesis. GSAS-II was then used to determine the potential unit cells.³³ The determined unit cells and their scattering curves were observed in comparison to the peaks in the experimental scattering curves and the three proposed unit cells with peaks most similar to the experimental scattering peaks were selected and saved.

Results and Discussion

I. Experimental scattering of $[\text{Ir}_2(\text{dimen})_4][\text{X}]_2$ (**1-X**) at beamline 11-ID-B

The well-defined peaks in the scattering curves of **1-X** in the presence of both the hexafluorophosphate (PF_6) and tetraphenylborate (BPh_4) counterions indicate that the structure of these complexes is crystalline (Figure 11). In contrast, the relatively flat and undefined curve displayed in the scattering of **1-Cl** suggests that **1-Cl** is not crystalline (Figure 11).

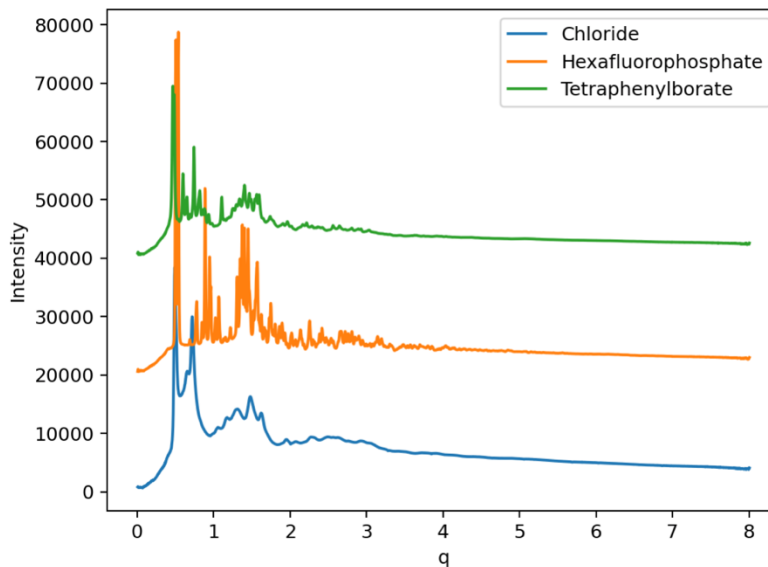


Figure 11. The scattering curves of $[\text{Ir}_2(\text{dimen})_4][\text{X}]_2$ (**1-X**) where X is the chloride (**1-Cl**), hexafluorophosphate (PF_6 , **1-PF₆**), or tetraphenylborate (BPh_4 , **1-BPh₄**) counterion.

II. $[\text{Ir}_2(\text{dimen})_4][\text{PF}_6]_2$ (**1-PF₆**)

Because **1-PF₆** and **1-BPh₄** have been analyzed using X-ray diffraction previously, the literature diffraction pattern can be analyzed.¹⁰ Additionally, previously published scattering curves and their unit cells can be used as a basis for generating a variety of unit cells corresponding to the experimental scattering curve. When comparing the literature spectrum of **1-PF₆** to our experimentally determined spectrum, the peaks seem to line up well with the exception of a few

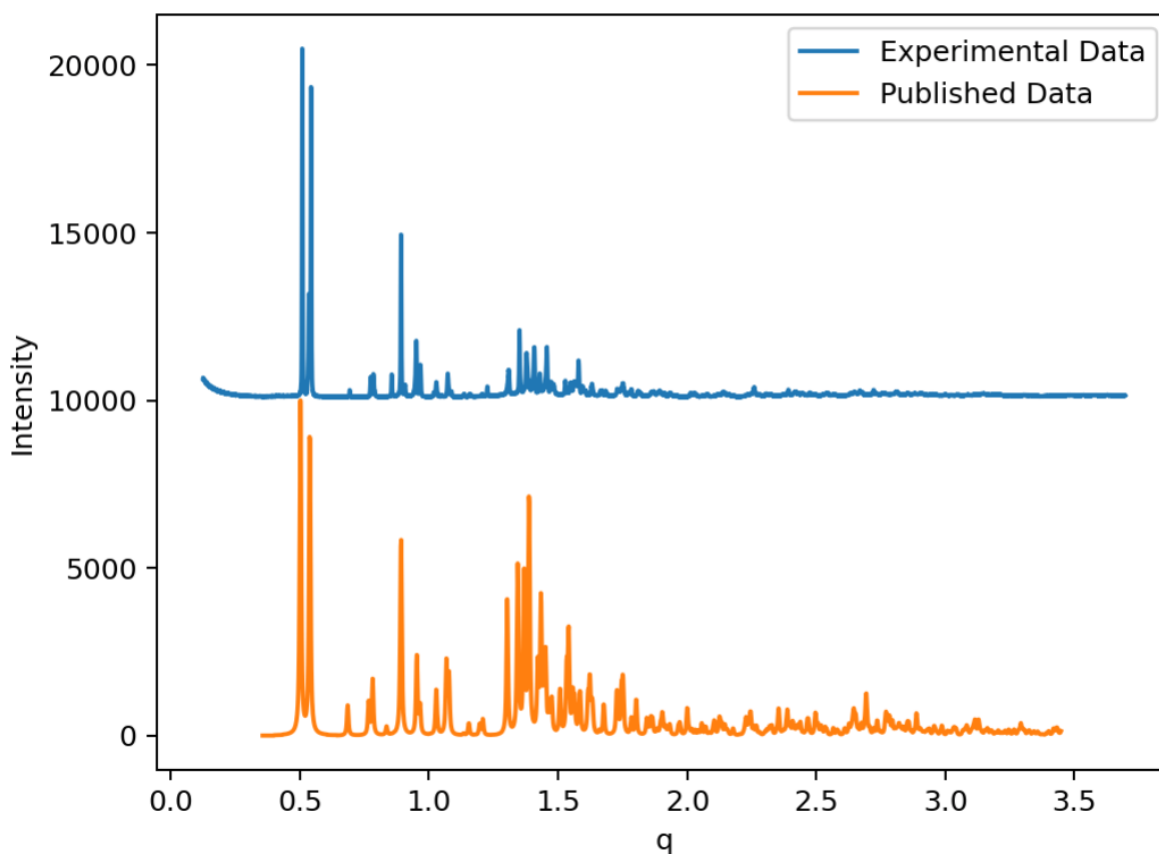


Figure 12. Scattering curves of 1-PF₆ obtained experimentally in this work and from the structural database.

peaks found between 1.3 and 1.7 in the q -range (Figure 12). The similarities between these spectra indicates that they likely have similar structures and therefore similar unit cells. Gray *et al.* reported that the unit cell was best modeled using a triclinic cell. This prompted further analysis and prediction of a unit cell using triclinic geometry.¹⁰ However, GSAS-II was unable to predict a unit cell using triclinic symmetry.¹⁰ Consequently, our experimental scattering pattern was quantitatively compared to the literature pattern published by Gray *et al.* using a Rietveld Plot in GSASII.

The Rietveld Plot indicates that, while there are some differences between peak intensities between our experimental pattern and literature scattering data, the atoms tend to be packed in a way that cause the similar scattering in both our data and that of Gray (Figure 13). This indicates

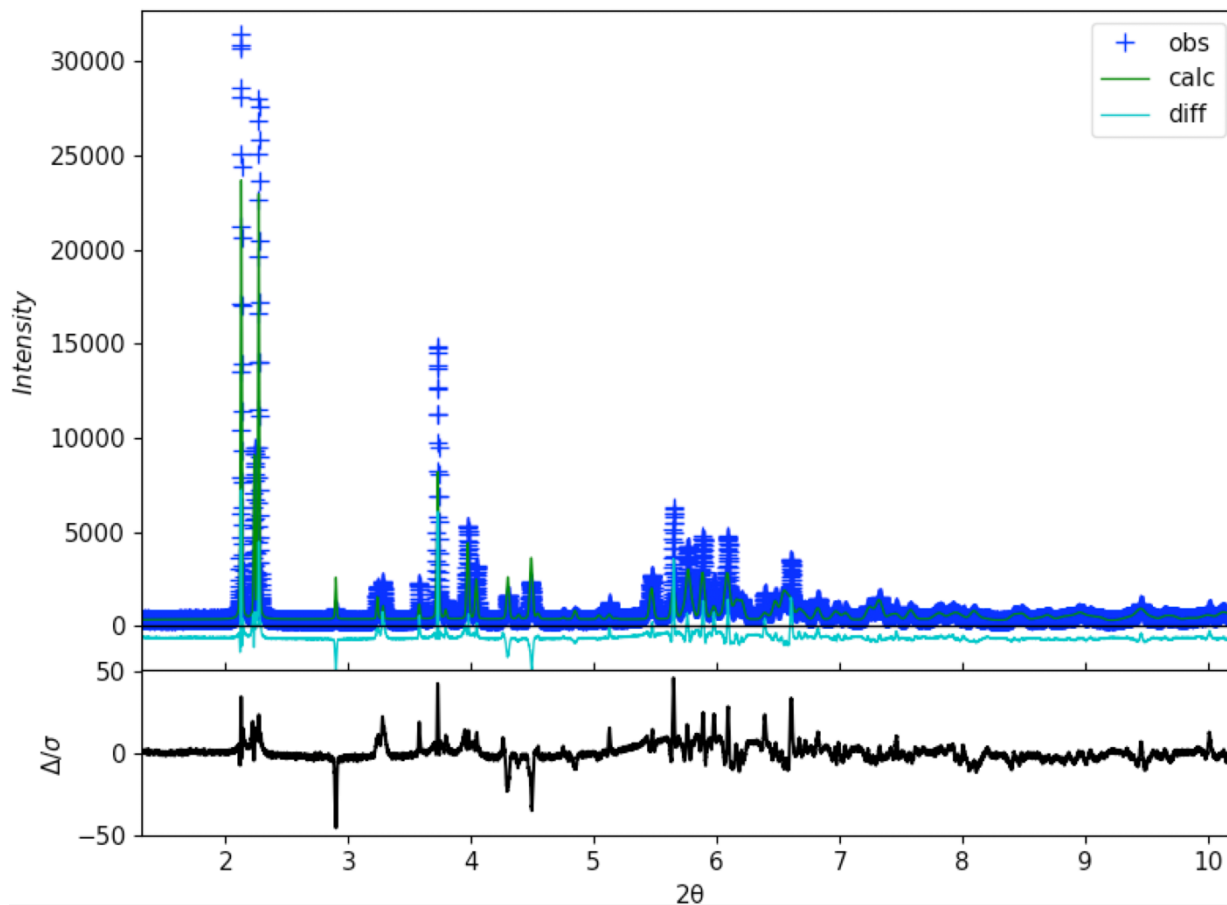


Figure 13. The Rietveld Plot of $[\text{Ir}_2(\text{dimen})_4][\text{PF}_6]_2$. ($\chi^2 = 18.86$).

that the unit cells exhibit similar planes, which, in turn, cause the scattering curves to resemble one another. Because of this, we can conclude that the structure and packing of 1- PF_6 in our sample is almost identical to that of Gray *et al.*

III. $[\text{Ir}_2(\text{dimen})_4][\text{BPh}_4]_2 \cdot \mathbf{1-BPh}_4$

Unlike the spectrum of $\mathbf{1-PF}_6$, the $\mathbf{1-BPh}_4$ scattering curve exhibits several differences from the literature spectrum (Figure 14).¹⁰ This suggests that the packing of $\mathbf{1-BPh}_4$ is different in our sample than it was in the sample used to obtain the literature spectrum. While this could be attributed to small differences in methods of synthesis, that is unlikely. Because the dimen ligand is asymmetrical, the differences in spectra are more likely a result of dimen ligands binding iridium atoms with orientations and orientational patterns that are different from that observed in work

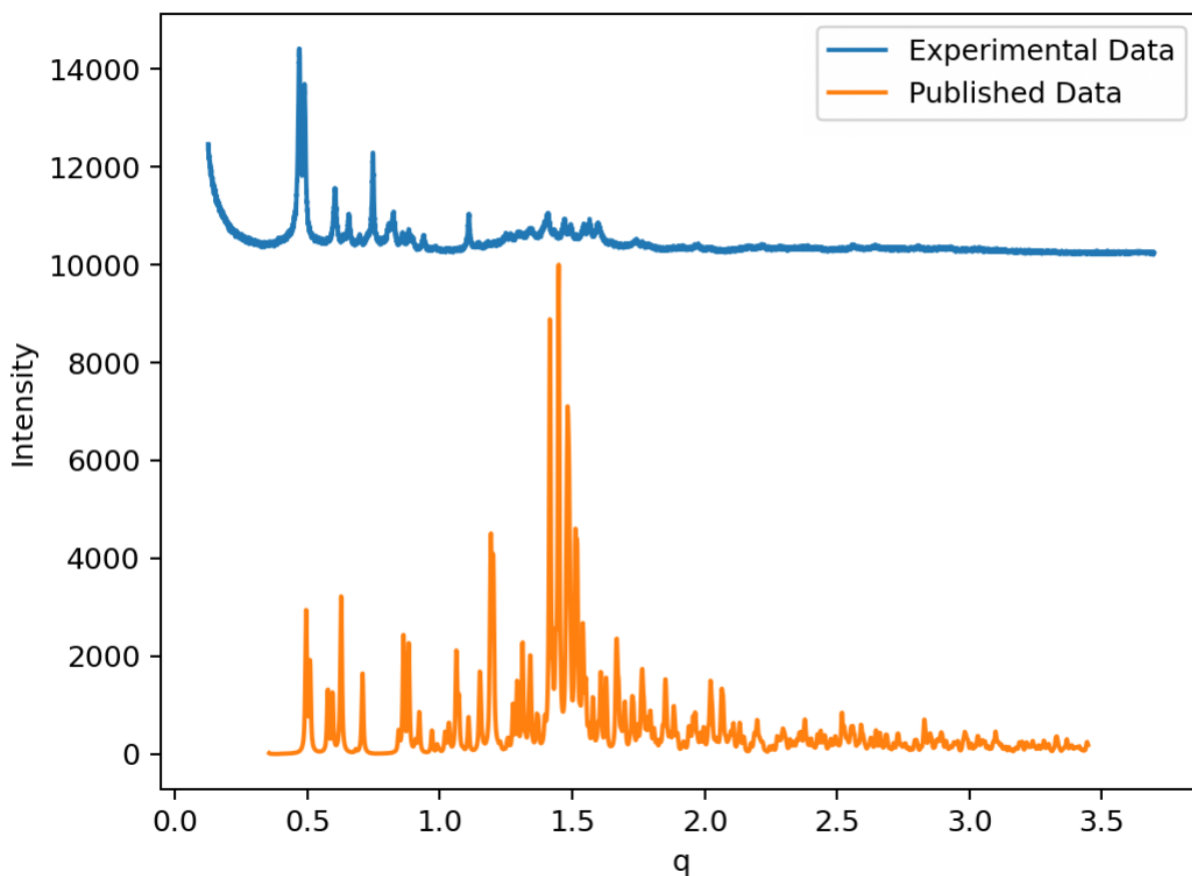


Figure 14. The scattering curves of $[\text{Ir}_2(\text{dimen})_4][\text{BPh}_4]_2$ determined experimentally and obtained from the structural database.

published by Gray *et al.* These differences are especially apparent in the q range of $1\text{-}2 \text{ \AA}^{-1}$.¹⁰ Additionally, the two intense peaks observed at about 0.5 in all samples of $\mathbf{1-X}$, regardless of counterion, are slightly shifted from one another in $\mathbf{1-BPh}_4$ where they were exactly lined up in

the experimental and literature curves exhibited by **1-PF₆**. Additionally, the peak intensities vary greatly, thus suggesting that the scattered waves are interacting differently and causing the scattering intensities and patterns to differ (Figure 14). These differences in scattering indicate that the packing of the complex is different.

Given the unit cell for **1-BPh₄** determined by Gray *et al.* and the general structure of the iridium complex, orthorhombic and tetragonal geometry were used to predict unit cells. Scattering curves predicted by primitive orthorhombic unit cells tended to most closely resemble the experimentally determined scattering curve. After comparing several predicted scattering curves with the experimentally determined scattering curve, a few unit cells were determined to exhibit the best packing. Interestingly, the calculated unit cells have volumes of 5216.144 Å³ and 5352.982 Å³ whereas the literature unit cell had a volume of 17592.7 Å³ (Table 1).¹⁰

TABLE 1. The dimensions and space group of the predicted unit cells and the literature unit cell. Values of a, b, and c correspond to the (100), (010), and (001) planes respectively.

Unit Cell	Space Group	Volume (Å ³)	Dimensions		
			a (Å)	b (Å)	c (Å)
BPh4_5198R	Pmmm	5216.144	9.29	13.36	42.04
BPh4_5354R	Pmmm	5354.982	10.39	13.38	38.48
Literature Cell	Pbca	17592.7	19.32	29.45	30.92

This is a stark difference and indicates that our predicted unit cells exhibit less symmetry than the literature unit cell but can be translationally replicated more frequently throughout the sample.

The predicted unit cells were unable to predict the structure of **1-PF₆** within the cell. However, it did predict the locations of some atoms within the cell. While this isn't particularly

useful, it is worthwhile to compare and analyze the planes from which the light diffracted and compare them to approximate distances within the cell.

Other than the indices of the unit cell, the most noticeable peaks in the experimental spectrum appear at distances of $d = 12.8$, $d = 9.6$, $d = 7.7$, $d = 7.1$, $d = 6.7$, $d = 5.6$, $d = 4.5$, and $d = 4.3$. There are notable peaks near all of these locations, each of which correspond to calculated planes.

TABLE 2. A comparison of the peaks at experimentally determined d - and Q -values to the corresponding planes of proposed unit cells BPh4_5354R and BPh4_5198R.

d (Å)	q -value (Å ⁻¹)	Corresponding Planes	
		BPh4_5354R	BPh4_5198R
13.398	0.469	(010)	(010)
12.819	0.490	(003)	(011)
10.406	0.604	(100)	(004)
9.566	0.657	(004)	(100)
7.613	0.825	(005)	(110)
7.099	0.885	(104)	(015)
6.685	0.940	(015)	(020)
5.659	1.110	(120)	(115)
4.457	1.410	(030)	(027)
4.271	1.471	(009)	(126)

The peaks corresponding to the planes calculated by the proposed unit cells, BPh4_5354R and BPh4_5198R, seem to be very different from one another (Table 2). This is to be expected

because the volumes, and thus the planes within the unit cell, differ slightly. However, some planes appear to correspond to the same, or similar peaks. For example, the (010) plane corresponds to the peak at 13.398 Å in both models (Table 2). Additionally, the calculated peaks corresponding to plane (015) have a horizontal difference of 0.055 in q-space (Table 2). These similarities between peaks allow us to hypothesize that **1-(BPh₄)** packed such that a defined unit cell could be determined to have about 1/3 the volume of that determined by Gray, *et al.* This means that the unit cells we calculated have less symmetry than the cell calculated by Gray *et al.*, which supports our hypothesis that the ligands bond with an orientational pattern different to that observed previously. However, due to a lack of data and time, we can draw no conclusions regarding the exact dimensions of the unit cell and the locations of atoms within the cell.

Conclusion

In this project, we utilized X-ray diffraction to obtain scattering curves of $\text{Ir}_2(\text{dimen})_4^{2+}$ (**1**) precipitated with chloride, hexafluorophosphate (PF_6) and tetraphenylborate (BPh_4) counterions. $[\text{Ir}_2(\text{dimen})_4][\text{Cl}]_2$ was determined to be not crystalline while both $[\text{Ir}_2(\text{dimen})_4][\text{PF}_6]_2$ (**1-PF₆**) and $[\text{Ir}_2(\text{dimen})_4][\text{BPh}_4]_2$ (**1-BPh₄**) were determined to be crystalline. **1-PF₆** exhibited a diffraction pattern almost identical to that of the published diffraction pattern. Because structure is directly related to the exhibited scattering pattern, these similarities indicate that the experimentally observed packing and structure of **1-PF₆** is the same as the previously reported structure. Contrastingly, the scattering curve, and consequently the packing, of **1-BPh₄** was significantly different than the packing previously observed by Gray *et al.* This means that the structure of **1-BPh₄** is different than previously observed. **1-BPh₄** was hypothesized to have a unit cell with a volume around 5300 \AA^3 , a volume about $1/3$ of that previously determined by Gray *et al.* While this finding is useful, there was insufficient time to determine the exact structure of $[\text{Ir}_2(\text{dimen})_4][\text{BPh}_4]_2$ within the unit cell.

In the future, the collected scattering pattern for **1-PF₆** and **1-BPh₄** should be more quantitatively analyzed to obtain a Rietveld plot that better fits the previously published scattering pattern. This will allow us to compare the two scattering curves more quantitatively to one another. Additionally, more analysis using GSASII should be conducted to obtain a unit cell that best describes the packing of **1-BPh₄**. Understanding the packing of $[\text{Ir}_2(\text{dimen})_4][\text{BPh}_4]_2$ that resulted in both curves may give more understanding as to the solid-state UV-visible spectrum of **1-BPh₄**. Additionally, it may give more insight into the structures of $\text{Ir}_2(\text{dimen})_4^{2+}$ observed in solution.

In order to better understand the way that $\text{Ir}_2(\text{dimen})_4^{2+}$ behaves in solution, it is crucial to first fully understand the way that $[\text{Ir}_2(\text{dimen})_4][\text{BPh}_4]_2$ behaves as a solid. Not only will this allow

for better understanding of structures of **1-BPh₄** as a solid and Ir₂(dimen)₄²⁺ in solution, but it could also allow for better understanding of how d⁸ square planar dimers exist in solution, thus providing a gateway to improving the reactions and catalysis that could make hydrogen fuel a more foreseeable alternative to fossil fuels.

References

- (1) Gray, H. B.; Maverick, A. W. Solar Chemistry of Metal Complexes. *Science* **1981**, *214* (4526), 1201–1205.
- (2) Hoffman, P.; Dorgan, B. Why Hydrogen? The Grand Picture. In *Tomorrow's Energy: Hydrogen, Fuel Cells, and the Prospects for a Cleaner Planet*; MIT Press, 2012; pp 1–17.
- (3) Gray, H. B.; Zális, S.; Vlček, A. Electronic Structures and Photophysics of D8-D8 Complexes. *Coord. Chem. Rev.* **2017**, *345*, 297–317.
<http://dx.doi.org/10.1016/j.ccr.2017.01.008>.
- (4) Jasim, N. A.; Perutz, R. N. Hydrogen Bonding in Transition Metal Complexes: Synthesis, Dynamics, and Reactivity of Platinum Hydride Bifluoride Complexes. *J. Am. Chem. Soc.* **2000**, *122*, 8685–8693.
- (5) Sathyanarayana, D. N. Absorption and Emission of Electromagnetic Radiation. In *Electronic Absorption Spectroscopy and Related Techniques*; Universities Press (India) Limited, 2001; pp 5–7.
- (6) *Solar Radiation & Photosynthetically Active Radiation*; Fondriest Environmental, Inc., 2014.
- (7) Haldrup, K.; Harlang, T.; Christensen, M.; Asmus, D.; Brandt van Driel, T.; Skov Kjær, K.; Harrit, N.; Vibenholt, J.; Guerin, L.; Wulff, M.; Meedom Nielson, M. Bond Shortening (1.4 Å) in the Singlet and Triplet Excited States of [Ir₂(Dimen)₄]²⁺ in Solution Determined by Time-Resolved X-Ray Scattering. *Inorg. Chemistry* **2011**, *50*, 9329–9336.
<https://doi.org/10.1021/ic2006875>.
- (8) Hartstock, R. W.; Zhang, W.; Hill, M. G.; Sabat, B.; Gaffney, K. J. Characterizing the Deformational Isomers of Bimetallic Ir₂(Dimen)₄²⁺ (Dimen = 1,8-Diisocyano-p-

- Menthane) with Vibrational Wavepacket Dynamics. *J. Phys. Chem.* **2011**, *115*, 2920–2926. <https://doi.org/10.1021/jp1114493>.
- (9) Hunter, B. M.; Villahermosa, R. M.; Exstrom, C. L.; Hill, M. G.; Mann, K. R.; Gray, H. B. M–M Bond-Stretching Energy Landscapes for M₂(Dimen)₄²⁺ (M = Rh, Ir; Dimen = 1,8-Diisocyanomenthane) Complexes. *Inorg. Chem.* **2012**, *51*, 6898–6905. <https://doi.org/10.1021/ic300716q>.
- (10) Exstrom, C. L.; Britton, D.; Mann, K. R.; Hill, M. G.; Miskowski, V. M.; Schaefer, W. P.; Gray, H. B.; Lamanna, W. M. Structures of [M₂(Dimen)₄](Y)₂ (M = Rh, Ir; Dimen = 1,8-Diisocyanomenthane; Y = PF₆, Tetrakis[3,5-Bis(Trifluoromethyl)Phenyl]Borate, B(C₆H₅)₄) Crystals Featuring an Exceptionally Wide Range of Metal–Metal Distances and Dihedral Twist Angles. *Inorg. Chem.* **1996**, *35* (3), 549–550.
- (11) Atkins, P.; de Paula, J. Molecular Spectroscopy 2: Electronic Transitions. In *Physical Chemistry*; W. H. Freeman and Company New York, 2006; Vol. 8, pp 481–505.
- (12) Atkins, P.; de Paula. Molecular Spectroscopy 1: Rotational and Vibrational Spectra. In *Physical Chemistry*; W. H. Freeman and Company New York, 2006; Vol. 8, pp 471–476.
- (13) Pfennig, B. W. Crystal Field Theory. In *Principles of Inorganic Chemistry*; Wiley, 2015; pp 512–525.
- (14) Pfennig, B. W. The VSEPR Model. In *Principles of Inorganic Chemistry*; Wiley, 2015; pp 156–170.
- (15) Harvey, E. L.; Stiegman, A. E.; Vlček, A.; Gray, H. B. Dihydridotetrakis(Pyrophosphito(2-))Diplatinate(III). *J. Am. Chem. Soc.* **1987**, *109*, 5233–5235.

- (16) Vlček, A.; Gray, H. B. Binuclear Platinum(II) Photochemistry. Reactions of Organometallic Hydrides with Electronically Excited Tetrakis(Pyrophosphito)Diplatinate(II). *Inorg. Chem.* **1987**, *26*, 1997–2001.
- (17) Rohrer, G. Generalization about Crystal Structures Based on Periodicity. In *Structure and Bonding in Crystalline Materials*; Cambridge University Press, 2001.
- (18) Marín, C.; Diéguez, E. X-Ray Diffraction by Crystal Lattices. In *Orientation of Single Crystal by Back-Reflection Laue Pattern Simulations*; World Scientific Publishing Co. Pte. Ltd., 1999; pp 1–18.
- (19) Grandy, D. A. The Double-Slit Experiment. In *Everyday Quantum Reality*; Indiana University Press, 2010; pp 49–62.
- (20) Prutchi, D.; Prutchi, S. R. Chapter 1: Light as a Wave. In *Exploring Quantum Physics Through Hands-On Projects*; John Wiley & Sons, Inc., 2012.
- (21) NekoJaNekoJa~commons wiki. *Double-Slit*; 2005.
- (22) Atkins, P.; de Paula, J. Molecular Structure. In *Physical Chemistry*; W. H. Freeman and Company New York, 2006; Vol. 8, pp 362–398.
- (23) Pfennig, B. W. Metallic Bonding. In *Principles of Inorganic Chemistry*; Wiley, 2015; pp 339–350.
- (24) Dang Ngoc Change, C. *Braggs Law*; 2011.
- (25) Toney, M. Introduction to Synchrotron X-Ray Scattering Techniques.
- (26) Mehta, A. Introduction to Reciprocal Space.
- (27) Atkins, P.; de Paula, J. Materials 2: The Solid State; W. H. Freeman and Company New York, 2006; Vol. 8, pp 697–710.
- (28) Dang Ngoc Change, C. *Indices_miller_plan_definition*; 2009.

- (29) AdvancedPhotonSource. *The Advanced Photon Source at Argonne National Laboratory*; 2022.
- (30) Sykes, A. G. *Synthesis, Reactivity and Electronic Spectral Properties of Iridium 1,8-Diisocyanomethane Complexes Containing Group IB Coinage Metals*, University of Minnesota, 1990.
- (31) Vlček, A. [Ir₂(Dimen)₄][TFPB]₂ and [Ir₂(TMB)₄][TFPB]₂, 2021.
- (32) Mathiesen, J. K.; Quinson, J.; Dworzak, A.; Vosch, T.; Juelsholt, M.; Kjær, E. T. S.; Schröder, J.; Kirkensgaard, J. J. K.; Oezaslan, M.; Arenz, M.; Jensen, K. M. Ø. Insights from In Situ Studies on the Early Stages of Platinum Nanoparticle Formation. *J. Phys. Chem. Lett.* **2021**, *12*, 3224–3231.
- (33) Toby, B. H.; Von Dreele, R. B. GSAS-II: The Genesis of a Modern Open-Source All Purpose Crystallography Software Package. *J. Appl. Crystallogr.* *46* (2), 544–549. <https://doi.org/doi:10.1107/S0021889813003531>.